Chinese Physics Letters

LETTER

Intermediate-State Coulomb-Corrected Strong-Field Approximation for Nonsequential Double Ionization

Cite as: Chunli Miao *et al*. 2026 *Chin. Phys. Lett.* **43** 080301

DOI CSTR

Recommended Articles

Nonsequential Double Ionization by Circularly Polarized Laser Pulses: Recollisions Triggered by Nanotips
Xuan Luo, Xiaohu Ji, Liguang Jiao, Aihua Liu, and Xueshen Liu
Chin. Phys. Lett. **42**, 070301 (2025)

Precise Control of the Recollision Dynamics in Nonsequential Double Ionization by Spatially Inhomogeneous Few-Cycle Negatively Chirped Laser Pulses
Yingbin Li *et al*.
Chin. Phys. Lett. **42**, 053703 (2025)

***In situ* Measurement of Intense Optical Fields via Strong Field Ionization**
Fan Xiao, Li Wang, Guangru Bai, Zhigang Zheng, Xu Sun, Tiefeng Ji, Yuchen Sun, Jiacan Wang, Xiaowei Wang, and Zengxiu Zhao
Chin. Phys. Lett. **42**, 043701 (2025)

Rydberg-State Excitation and Ionization of Argon Atoms Subject to Strong Circularly Polarized Two-Color Few-Cycle Laser Fields
Zhiqiang Wang, Wei Quan, Yanlan Wang, Xiaolei Hao, Jing Chen, and Xiaojun Liu
Chin. Phys. Lett. **42**, 053701 (2025)

***In Situ* Attosecond Probing of Strong-Field Ionization Dynamics via a Transient Plasma Grating**
Ye Ma, Cong-Sen Meng, Zhi-Hui Lyu, Yuan Zhang, Dong-Wen Zhang, Xu Sun, Hai-Zhong Wu, Xiao-Wei Wang, Zeng-Xiu Zhao, and Jian-Min Yuan
Chin. Phys. Lett. **42**, 120303 (2025)

A series journal of Chinese Physical Society distributed by IOP Publishing

Chinese Physics Letters

Chin. Phys. Lett. **43** 080301 (2026)

LETTER

DOI: 10.1088/0256-307X/43/8/080301
CSTR: 32039.14.0256-307X.43.8.080301

Intermediate-State Coulomb-Corrected Strong-Field Approximation for Nonsequential Double Ionization

Chunli Miao[1,†], Hao Ren[1,†], Chan Li[1], Jingyu Zhang[1,*], Zheng Shu[1], Xiaolei Hao[1,*], Weidong Li[2], and Jing Chen[3,4,*]

[1]Institute of Theoretical Physics, State Key Laboratory of Quantum Optics Technologies and Devices, Shanxi University, Taiyuan 030006, China
[2]Shenzhen Key Laboratory of University Laser and Advanced Material Technology, and College of Engineering Physics, Shenzhen Technology University, Shenzhen 518118, China
[3]Department of Modern Physics, and Hefei National Research Center for Physical Sciences at the Microscale and School of Physical Sciences, University of Science and Technology of China, Hefei 230026, China
[4]Hefei National Laboratory, Hefei 230088, China

[†]These authors contributed equally to this work.
[*]Corresponding authors. Email: zhangjingyu@sxu.edu.cn; xlhao@sxu.edu.cn; chenjing@ustc.edu.cn

We present a refined strong-field approximation (SFA) theory incorporating the intermediate-state Coulomb interaction for nonsequential double ionization (NSDI). By introducing the Coulomb−Volkov wave function into the intense-field many-body S-matrix theory, we develop an intermediate-state Coulomb-corrected strong-field approximation (ICSFA) to address the long-standing deficiency of neglecting the Coulomb potential acting on the recolliding electron. Using the recollision excitation with subsequent ionization (RESI) mechanism in helium as a benchmark, we perform a systematic comparison between the conventional SFA and the ICSFA. The correlated electron momentum distributions (CEMDs) calculated via ICSFA show a significant redistribution of electron yield toward high-momentum regions and off-axis quadrants, which aligns quantitatively with experimental observations, whereas the SFA fails to reproduce these features. Concurrently, the joint energy distributions (JEDs) manifest a corresponding evolution. Analysis reveals that the Coulomb potential promotes large-angle scattering, thereby reshaping the CEMD and the JED. Furthermore, the ICSFA reveals a substantial enhancement of multiple-return recollision (MRR) trajectories, stemming from the combined effects of Coulomb focusing (manifested through the normalization factor) and the energy-dependent enhancement of the inelastic scattering cross-section. Our work establishes that the intermediate-state Coulomb interaction is indispensable for a quantitatively accurate description of strong-field correlated electron dynamics.

Introduction

Many-body correlations constitute a fundamental problem of broad interest across physics, chemistry, and materials science. In laser-induced atomic and molecular physics, ultrafast intense laser fields provide a unique and highly controllable platform for accessing correlation effects that are inaccessible under conventional conditions. Electron-electron correlation, in particular, is pivotal to understanding a host of nonperturbative strong-field phenomena, ranging from high-harmonic generation (HHG) [1−4] and non-sequential double ionization (NSDI) (for reviews, see Refs. [5−7]), to molecular ionization and dissociation [8−13]. Recent advances in attosecond metrology have further extended this reach to the investigation of laser-driven quantum correlations and entanglement [14−20]. Among these processes, NSDI stands out as a paradigmatic process for investigating electron correlation. Historically, several mechanisms have been proposed to explain NSDI, such as shake-off (SO) [21], collective tunneling (CT) [22], sequential double ionization (SDI) [23,24], recollision impact-ionization (RII) [25,26], recollision-excitation with subsequent ionization (RESI) [27,28]. While extensive studies have established that laser-induced inelastic recollision (RII and RESI) [25,29] dominates NSDI in the long-wavelength regime (near- and mid-infrared), alternative mechanisms may prevail under different conditions.

Theoretically, the intense-field many-body S-matrix theory (IMST) [30], which is well known in collision physics [31,32], has emerged as a powerful and systematic nonperturbative framework for describing strong-field many-body dynamics. It mitigates the prohibitive computational cost associated with solving many-body problems. A central advantage of IMST lies in its diagrammatic approach, which enables a unified treatment of complex strong-field phenomena by handling multiple interaction potentials, including electron-electron correlation, laser-field coupling, and the intermediate rearrangement Hamiltonian, on an equal footing. As a result, IMST has successfully accounted for numerous key experimental observations [33−35] and played a decisive role in elucidating NSDI mechanisms [27,36−39]. In recent years, renewed interest in IMST has been stimulated by its integration with concepts from quantum optics and quantum information theory [40−42]. These developments indicate the sustained relevance of IMST and suggest considerable potential for further refinement and extension in new physical contexts and application scenarios.

Despite these achievements, conventional implementations of the S-matrix framework still suffer from a well-recognized limitation, namely the inadequate treatment of the long-range Coulomb interaction acting on the liberated electron. In practice, this shortcoming most commonly arises within the strong-field approximation (SFA) [43−45], where the continuum electron is described by plane-wave Volkov states and the Coulomb potential is neglected after ionization. While this approximation greatly simplifies the theoretical treatment, it can lead to pronounced discrepancies with experimental measurements. Specifically, the long-range Coulomb interaction induces Coulomb focusing, which significantly enhances the contribution of multiple-return recollision (MRR) trajectories [10,46,47]. Extensive experimental and theoretical studies have demonstrated that Coulomb effects are indispensable for a quantitatively accurate description of strong-field dynamics, particularly in reproducing the correlated photoelectron momentum distributions [39,48−50]. A proper treatment of the Coulomb interaction is therefore indispensable for a quantitatively

Received 18 May 2026; accepted 8 July 2026; published 19 August 2026
© 2026 Chinese Physical Society and IOP Publishing Ltd. All rights, including for text and data mining, AI training, and similar technologies, are reserved.

Check for updates

accurate and physically consistent description of strong-field correlated electron dynamics. These considerations motivate the development of improved S-matrix formulations in which the Coulomb interaction is incorporated more rigorously, thereby providing a more reliable connection between theory and experiment.

In this paper, we derive a complete series expansion for the atomic NSDI process by applying the Coulomb−Volkov correction to the intermediate state within the framework of the IMST. This series inherently incorporates mechanisms historically proposed to account for NSDI, including SO, SDI, RII, and RESI. In recent years, the quest to understand the microscopic dynamics of RESI has led to a paradigm shift from simple classical trajectory models to sophisticated quantum mechanical treatments. Specifically, the application of the saddle-point method within the SFA has revealed that the RESI process is dominated by the coherent superposition of multiple quantum paths [51]. Furthermore, the utilization of bichromatic driving fields has emerged as a powerful experimental knob to precisely control the strong-field quantum interference and rescattering dynamics inherent in RESI [52,53]. Taking the RESI process as the example, we present a systematic theoretical investigation into the role of the Coulomb interaction in the intermediate stage of strong-field double ionization. The S-matrix formalism for RESI process explicitly describes the three-step transition: ionization of the first electron (e_1), inelastic recollision accompanied by excitation of the residual ion, and the subsequent ionization of the second electron (e_2). This formulation allows for a controlled and quantitative comparison between two distinct descriptions of the returning electron, namely the conventional SFA and the intermediate-state Coulomb-corrected strong-field approximation (ICSFA), in which the recolliding electron is described by a Coulomb–Volkov state during the recollision process. By computing the correlated electron momentum distributions (CEMDs) within both approaches and comparing them with experimental measurements reported in Ref. [54], we demonstrate that the ICSFA yields better agreement with the observed momentum structures. Beyond reproducing experimental observables, our analysis reveals the underlying physical mechanism responsible for this improvement. This work establishes a framework for the accurate description of the Coulomb interaction in strong-field correlated electron dynamics.

Methods

Traditional Quantum S-Matrix Theory

For a two-active-electron atomic system interacting with an external laser field, the corresponding Hamiltonian within the dipole approximation and in the length gauge is given by (atomic units $\hbar = m_e = |e| = 1$ are used)

$$H(t) = \frac{\hat{\boldsymbol{p}}_1^2 + \hat{\boldsymbol{p}}_2^2}{2} - \frac{Z}{r_1} - \frac{Z}{r_2} + \frac{1}{r_{12}} + (\boldsymbol{r}_1 + \boldsymbol{r}_2)\cdot\boldsymbol{E}(t), \tag{1}$$

where $\hat{\boldsymbol{p}}_j$ and $\boldsymbol{r}_j$ $(j = 1,2)$ denote the momentum operator and position vector of the jth electron, respectively, and Z represents the effective nuclear charge. The term $r_{12} = |\boldsymbol{r}_1 - \boldsymbol{r}_2|$ describes the inter-electronic separation, while $\boldsymbol{E}(t)$ is the time-dependent laser electric field. The Hamiltonian comprises the kinetic energy of both electrons, the electron–nucleus binding potential, the electron–electron Coulomb interaction, and the dipole interaction between the electrons and the external field.

The transition amplitude from the initial state Ψ_i at time t_i, prior to the laser pulse, to the final state Ψ_f at time t_f, after the termination of the laser pulse can be expressed as

$$M_{fi} = \lim_{t_f\to\infty, t_i\to-\infty} \langle\Psi_f(t_f)|U(t_f,t_i)|\Psi_i(t_i)\rangle, \tag{2}$$

where $U(t_f,t_i)$ is the full evolution operator corresponding to the total Hamiltonian in Eq. (1). Following the many-body S-matrix formalism [30], the time-evolution operator $U(t_f,t_i)$ can be systematically expanded by partitioning the total Hamiltonian. We first adopt the conventional decomposition

$$H(t) = H_i(t) + V_i(t), \tag{3}$$

with

$$\begin{aligned} H_i(t) &= \frac{\hat{\boldsymbol{p}}_1^2 + \hat{\boldsymbol{p}}_2^2}{2} - \frac{Z}{r_1} - \frac{Z}{r_2} + \frac{1}{r_{12}}, \\ V_i(t) &= (\boldsymbol{r}_1 + \boldsymbol{r}_2)\cdot\boldsymbol{E}(t), \end{aligned} \tag{4}$$

where $H_i(t)$ describes the field-free unperturbed target Hamiltonian and $V_i(t)$ represents the interaction with the external laser field.

Under this partition, the total evolution operator can be expanded as

$$U(t_f,t_i) = U_i(t_f,t_i) - i\int_{t_i}^{t_f} dt_1\, U(t_f,t_1)V_i(t_1)U_i(t_1,t_i), \tag{5}$$

where the time evolution operator $U_i(t_f,t_i)$ corresponds to the field-free Hamiltonian $H_i(t)$.

To facilitate the description of specific physical mechanisms, it is advantageous to introduce an alternative partitioning scheme:

$$H(t) = H_0(t) + V_0(t), \tag{6}$$

where the specific forms of $H_0(t)$ and $V_0(t)$ may be chosen flexibly depending on the dynamical process under consideration. This freedom allows for tailored descriptions of distinct ionization mechanisms and significantly facilitates the corresponding calculations. The explicit definitions of $H_0(t)$ and $V_0(t)$ will be specified in subsequent subsections. We first present the formal expressions that are valid for arbitrary choices of these operators. Under this general partition, the evolution operator $U(t_f,t_1)$ appearing in Eq. (5) can be further expanded as

$$U(t_f,t_1) = U_0(t_f,t_1) - i\int_{t_1}^{t_f} dt_2\, U(t_f,t_2)V_0(t_2)U_0(t_2,t_1), \tag{7}$$

where $U_0(t_f,t_1)$ corresponds to $H_0(t)$. Substituting it into Eq. (5), we can obtain

$$\begin{aligned} U(t_f,t_i) = U_i(t_f,t_i) &- i\int_{t_i}^{t_f} dt_1\, U_0(t_f,t_1)V_i(t_1)U_i(t_1,t_i) \\ &- \int_{t_1}^{t_f} dt_2\, U(t_f,t_2)V_0(t_2) \\ &\times \int_{t_i}^{t_f} dt_1\, U_0(t_2,t_1)V_i(t_1)U_i(t_1,t_i). \end{aligned} \tag{8}$$

Inserting Eq. (8) into Eq. (2), the transition amplitude can be rewritten as

$$\begin{aligned} M_{fi} = \delta_{fi} &- i\int_{-\infty}^{\infty} dt_1 \langle\Psi_f(t_1)|V_i(t_1)|\Psi_i(t_1)\rangle \\ &- \int_{-\infty}^{\infty}\int_{t_1}^{\infty} dt_2 dt_1 \langle\Psi_f(t_f)|U(t_f,t_2) \\ &\times V_0(t_2)U_0(t_2,t_1)V_i(t_1)|\Psi_i(t_1)\rangle. \end{aligned} \tag{9}$$

Iterative substitution of the expansion in Eq. (9), specifically utilizing V_0' and U_0' in subsequent steps, yields the standard S-matrix series:

$$M_{fi}^{(1)} = -i\int_{-\infty}^{\infty} dt_1 \langle\Psi_f(t_1)|V_i(t_1)|\Psi_i(t_1)\rangle, \tag{10}$$

$$M_{fi}^{(2)} = -\int_{-\infty}^{\infty}\int_{t_1}^{\infty} dt_2 dt_1 \langle\Psi_f(t_2)|V_0(t_2)U_0(t_2,t_1)V_i(t_1)|\Psi_i(t_1)\rangle, \tag{11}$$

$$\begin{aligned} M_{fi}^{(3)} = i\int_{-\infty}^{\infty}\int_{t_1}^{\infty}\int_{t_2}^{\infty} &dt_3\, dt_2\, dt_1 \langle\Psi_f(t_3)|V_0'(t_3) \\ &\times U_0'(t_3,t_2)V_0(t_2)U_0(t_2,t_1)V_i(t_1)|\Psi_i(t_1)\rangle, \\ \cdots = \cdots, \end{aligned} \tag{12}$$

where V_0' and U_0' arise from subsequent iterations of the expansion

and may differ from V_0 and U_0, reflecting the freedom in choosing the Hamiltonian partition at different stages of the S-matrix construction.

The first-order S-matrix [Eq. (10)] describes the direct double-ionization process induced by the laser-electron interaction $V_{\rm i}$, corresponding to the shake-off mechanism [21]. The physical mechanisms of the second- and third-order terms depend on the specific choice of the partition $H(t)$ into $H_0(t)$ and $V_0(t)$, which determines the underlying ionization dynamics. These interpretations are discussed in detail in the following subsections. Higher-order terms of the S-matrix incorporate increasingly complex electron-field and electron-electron dynamics, underscoring the S-matrix formalism as a powerful theoretical framework for investigating intricate light-matter processes.

SFA

Within the SFA framework, a central approximation is the neglect of the Coulomb interaction between the recolliding electron and its parent ion once the electron is promoted to the continuum. Accordingly, $H_0(t)$ and $V_0(t)$ in the second partition of total Hamiltonian $H(t)$ induced in Eq. (6) are typically defined as

$$H_0^{(\rm V)}(t) = \frac{\widehat{\boldsymbol{p}}_1^2}{2} + \boldsymbol{r}_1\cdot\boldsymbol{E}(t) + \frac{\widehat{\boldsymbol{p}}_2^2}{2} - \frac{Z}{r_2}, \tag{13}$$

$$V_0^{(\rm V)}(t) = -\frac{Z}{r_1} + \frac{1}{r_{12}} + \boldsymbol{r}_2\cdot\boldsymbol{E}(t), \tag{14}$$

where $H_0^{(\rm V)}(t)$ serves as the reference Hamiltonian describing e_1 evolving in the laser field as a Volkov particle and e_2 remaining bound to the ionic core, while $V_0^{(\rm V)}(t)$ represents the residual perturbative interactions. The time-evolution operator corresponding to $H_0^{(\rm V)}$ is approximated as a direct product $U_0^{(\rm V)} = U_{\rm V}^{(1)}\otimes U_{\rm b}^{(2)}$, where $U_{\rm V}^{(1)}$ is the Volkov propagator for e_1 and $U_{\rm b}^{(2)}$ is the field-free time propagator for e_2.

The Volkov state, which is an eigenstate of a free electron in a laser field is characterized by the asymptotic momentum $\boldsymbol{k}$. In the length gauge, it is expressed as

$$\begin{aligned}\Phi_{\boldsymbol{k}}^{(\rm V)}(\boldsymbol{r},t) = (2\pi)^{-3/2}&\exp\{{\rm i}[\boldsymbol{k}+\boldsymbol{A}(t)]\cdot\boldsymbol{r}\}\\ &\times\exp\Big(-{\rm i}\int^t {\rm d}\tau\frac{[\boldsymbol{k}+\boldsymbol{A}(\tau)]^2}{2}\Big),\end{aligned} \tag{15}$$

where $\boldsymbol{A}(\tau)$ is the vector potential of the laser field.

Upon further iterative expansion of the evolution operator using the same partition defined in Eqs. (13) and (14) and assuming that the system is initially prepared in a product state of one-electron ground states and finally detected in a two-electron Volkov state with asymptotic momentum $\boldsymbol{p}_1$ and $\boldsymbol{p}_2$, the second- and third-order terms of S-matrix can be rewritten as

$$\begin{aligned}M_{\rm fi}^{(2)} = -\int_{-\infty}^{\infty}{\rm d}t_2\int_{t_1}^{\infty}{\rm d}t_1\int{\rm d}^3\boldsymbol{k}\\ \times\langle\Phi_{\boldsymbol{p}_1}^{(\rm V)}(\boldsymbol{r}_1),\Phi_{\boldsymbol{p}_2}^{(\rm V)}(\boldsymbol{r}_2)|V_0^{(\rm V)}|\Phi_{\boldsymbol{k}}^{(\rm V)}(\boldsymbol{r}_1),\psi'(\boldsymbol{r}_2)\rangle_{t_2}\\ \times\langle\Phi_{\boldsymbol{k}}^{(\rm V)}(\boldsymbol{r}_1),\psi'(\boldsymbol{r}_2)|V_{\rm i}|\psi(\boldsymbol{r}_1),\psi(\boldsymbol{r}_2)\rangle_{t_1},\end{aligned} \tag{16}$$

$$\begin{aligned}M_{\rm fi}^{(3)} = {\rm i}\int_{-\infty}^{\infty}{\rm d}t_3\int_{t_2}^{\infty}{\rm d}t_2\int_{t_1}^{\infty}{\rm d}t_1\int{\rm d}^3\boldsymbol{k}\\ \times\langle\Phi_{\boldsymbol{p}_1}^{(\rm V)}(\boldsymbol{r}_1),\Phi_{\boldsymbol{p}_2}^{(\rm V)}(\boldsymbol{r}_2)|V_0^{(\rm V)}|\Phi_{\boldsymbol{p}_1}^{(\rm V)}(\boldsymbol{r}_1),\psi''(\boldsymbol{r}_2)\rangle_{t_3}\\ \times\langle\Phi_{\boldsymbol{p}_1}^{(\rm V)}(\boldsymbol{r}_1),\psi''(\boldsymbol{r}_2)|V_0^{(\rm V)}|\Phi_{\boldsymbol{k}}^{(\rm V)}(\boldsymbol{r}_1),\psi'(\boldsymbol{r}_2)\rangle_{t_2}\\ \times\langle\Phi_{\boldsymbol{k}}^{(\rm V)}(\boldsymbol{r}_1),\psi'(\boldsymbol{r}_2)|V_{\rm i}|\psi(\boldsymbol{r}_1),\psi(\boldsymbol{r}_2)\rangle_{t_1},\end{aligned} \tag{17}$$

where ψ, ψ', and ψ'' denote the atomic ground state, the ionic ground state and an ionic excited state, respectively.

The second-order term $M_{\rm fi}^{(2)}$ [Eq. (16)] describes a two-step ionization process. According to Eq. (14), the interaction $V_0^{(\rm V)}$ contains three components, each corresponding to a distinct physical mechanism: (1) the component $\boldsymbol{r}_2\cdot\boldsymbol{E}(t)$ describes a SDI mechanism, in which e_1 is ionized to the Volkov state $\Phi_{\boldsymbol{k}}^{(\rm V)}$ by the laser field interaction $\boldsymbol{r}_1\cdot\boldsymbol{E}(t)$, followed by laser-driven ionization of e_2 via $\boldsymbol{r}_2\cdot\boldsymbol{E}(t)$; (2) the electron-electron interaction $1/r_{12}$ gives rise to a RII mechanism, where e_1 after being ionized via $\boldsymbol{r}_1\cdot\boldsymbol{E}(t)$, returns back to the core and liberates e_2 by the interaction $1/r_{12}$; (3) the component $-Z/r_1$ describes a pathway in which the returning electron interacts with the ionic potential to induce the ionization of e_2. This contribution is commonly neglected because of its comparatively low probability. Nevertheless, under certain conditions, its influence can become non-negligible, and our following re-examination indicates that this channel may have a significant impact on the dynamics.

The third-order term $M_{\rm fi}^{(3)}$ [Eq. (17)] describes a three-step ionization process and can be decomposed into nine distinct pathways, since each $V_0^{(\rm V)}$ consists of three terms. Among these, the RESI mechanism is of primary interest: e_1 is ionized to $\Phi_{\boldsymbol{k}}^{(\rm V)}$ at t_1 via $\boldsymbol{r}_1\cdot\boldsymbol{E}(t_1)$, subsequently recollides with the ion and excites e_2 at t_2 via the electron-electron interaction $1/r_{12}$, and finally e_2 is ionized at t_3 via $\boldsymbol{r}_2\cdot\boldsymbol{E}(t_3)$.

ICSFA

Although the SFA successfully captures the main features of NSDI, it neglects the $-Z/r_1$ term in V_0, describing the Coulomb field experienced by the first ionized electron in the intermediate state, and this omission may lead to serious problems. To achieve a more accurate description, we explicitly incorporate the intermediate-state Coulomb interaction by adopting the improved ICSFA.

Within this framework, the operators $H_0(t)$ and $V_0(t)$ in the second partition of total Hamiltonian $H(t)$ induced in Eq. (6) are defined as

$$H_0^{(\rm CV)}(t) = \frac{\widehat{\boldsymbol{p}}_1^2}{2} + \boldsymbol{r}_1\cdot\boldsymbol{E}(t) - \frac{Z}{r_1} + \frac{\widehat{\boldsymbol{p}}_2^2}{2} - \frac{Z}{r_2}, \tag{18}$$

$$V_0^{(\rm CV)}(t) = \frac{1}{r_{12}} + \boldsymbol{r}_2\cdot\boldsymbol{E}(t), \tag{19}$$

where $H_0^{(\rm CV)}(t)$ describes the compound system consisting of e_1 moving in the combined Coulomb and laser fields and e_2 bound to the ionic core, while $V_0^{(\rm CV)}(t)$ represents the residual perturbative interaction. The time-evolution operator corresponding to $H_0^{(\rm CV)}$ is given by $U_0^{(\rm CV)} = U_{\rm CV}^{(1)}\otimes U_{\rm b}^{(2)}$, where $U_{\rm CV}^{(1)}$ is the propagator for e_1 in the combined Coulomb and laser fields.

By employing the Coulomb–Born (CB) approximation [55,56], the intermediate continuum state of the recolliding electron corresponding to $U_{\rm CV}^{(1)}$ is described by the Coulomb–Volkov wave function $\Phi_{\boldsymbol{k}}^{(\rm CV)}(\boldsymbol{r},t)$ [57]:

$$\begin{aligned}\Phi_{\boldsymbol{k}}^{(\rm CV)}(\boldsymbol{r},t) = (2\pi)^{-3/2}N_k&\exp\{{\rm i}[\boldsymbol{k}+\boldsymbol{A}(t)]\cdot\boldsymbol{r}\}\\ &\times{}_1F_1(-{\rm i}\eta_k,1,-{\rm i}(kr+\boldsymbol{k}\cdot\boldsymbol{r}))\\ &\times\exp(-{\rm i}\int^t{\rm d}\tau\frac{[\boldsymbol{k}+\boldsymbol{A}(t)]^2}{2}),\end{aligned} \tag{20}$$

where ${}_1F_1(\cdot)$ is the confluent hypergeometric function, and

$$N_k = {\rm e}^{(\pi/2)\eta_k}\Gamma(1+{\rm i}\eta_k), \tag{21}$$

is the normalization coefficient. Here $\eta_k = Z/k$, with $k = |\boldsymbol{k}|$ denoting the magnitude of the intermediate momentum, and $\Gamma(\cdot)$ is the gamma function.

While a rigorous iterative expansion based on the $H_0^{(\rm CV)}$ and $V_0^{(\rm CV)}$ partition would generate Coulomb corrections for both intermediate and final propagation stages, we adopt a pragmatic hybrid approach. Given that e_1 typically exits the interaction volume rapidly following recollision, Coulomb effects in the post-recollision stage are deemed negligible. We therefore retain the standard SFA partition [Eqs. (13) and (14)] for the final-state evolution. Within this framework, the second- and third-order terms of S-matrix retain the same formal structure as in the SFA [Eqs. (16) and (17)], except that the intermediate Volkov states $\Phi_{\boldsymbol{k}}^{(\rm V)}$ are replaced by Coulomb–Volkov states $\Phi_{\boldsymbol{k}}^{(\rm CV)}$, and the intermediate operators $V_0^{(\rm V)}$ are replaced by $V_0^{(\rm CV)}$:

$$M_{\rm fi}^{(2)} = -\int_{-\infty}^{\infty}{\rm d}t_2\int_{t_1}^{\infty}{\rm d}t_1\int{\rm d}^3\boldsymbol{k} \times\langle\Phi_{\boldsymbol{p}_1}^{(\rm V)}(\boldsymbol{r}_1),\Phi_{\boldsymbol{p}_2}^{(\rm V)}(\boldsymbol{r}_2)|V_0^{(\rm CV)}|\Phi_{\boldsymbol{k}}^{(\rm CV)}(\boldsymbol{r}_1),\psi'(\boldsymbol{r}_2)\rangle_{t_2} \times\langle\Phi_{\boldsymbol{k}}^{(\rm CV)}(\boldsymbol{r}_1),\psi'(\boldsymbol{r}_2)|V_{\rm i}|\psi(\boldsymbol{r}_1),\psi(\boldsymbol{r}_2)\rangle_{t_1}, \tag{22}$$

$$M_{\rm fi}^{(3)} = {\rm i}\int_{-\infty}^{\infty}{\rm d}t_3\int_{t_2}^{\infty}{\rm d}t_2\int_{t_1}^{\infty}{\rm d}t_1\int{\rm d}^3\boldsymbol{k} \times\langle\Phi_{\boldsymbol{p}_1}^{(\rm V)}(\boldsymbol{r}_1),\Phi_{\boldsymbol{p}_2}^{(\rm V)}(\boldsymbol{r}_2)|V_0^{(\rm V)}|\Phi_{\boldsymbol{p}_1}^{(\rm V)}(\boldsymbol{r}_1),\psi''(\boldsymbol{r}_2)\rangle_{t_3} \times\langle\Phi_{\boldsymbol{p}_1}^{(\rm V)}(\boldsymbol{r}_1),\psi''(\boldsymbol{r}_2)|V_0^{(\rm CV)}|\Phi_{\boldsymbol{k}}^{(\rm CV)}(\boldsymbol{r}_1),\psi'(\boldsymbol{r}_2)\rangle_{t_2} \times\langle\Phi_{\boldsymbol{k}}^{(\rm CV)}(\boldsymbol{r}_1),\psi'(\boldsymbol{r}_2)|V_{\rm i}|\psi(\boldsymbol{r}_1),\psi(\boldsymbol{r}_2)\rangle_{t_1}. \tag{23}$$

Accordingly, the two components of $V_0^{(\rm CV)}$ correspond to two different physical pathways for $M_{\rm fi}^{(2)}$, namely SDI and RII. These processes are formally identical to those in the SFA, with the crucial difference that the intermediate continuum electron now evolves under the influence of the Coulomb potential. Similarly, $M_{\rm fi}^{(3)}$ can be decomposed into six different physical pathways within the ICSFA, among which the RESI mechanism remains dominant. This mechanism follows the same three-step sequence as in the SFA, but with a Coulomb-corrected intermediate propagation.

In the present work, we focus on the RESI mechanism as a representative case and systematically compare the CEMDs obtained from the SFA and ICSFA in order to elucidate the role of the Coulomb interaction in shaping the recollision dynamics.

RESI Formalism in SFA and ICSFA

In this subsection, we present the explicit formulation of the RESI mechanism within the aforementioned frameworks of SFA and ICSFA.

By applying closure relations and the explicit expressions for the time-evolution operators, the RESI transition amplitude can be reformulated as [36]

$$M(\boldsymbol{p}_1,\boldsymbol{p}_2) = \int_{-\infty}^{\infty}{\rm d}t_3\int_{-\infty}^{t_3}{\rm d}t_2\int_{-\infty}^{t_2}{\rm d}t_1\int{\rm d}^3\boldsymbol{k} \times V_{\boldsymbol{p}_2{\rm e}}V_{\boldsymbol{p}_1{\rm e},\boldsymbol{k}{\rm g}}V_{\boldsymbol{k}{\rm g}}{\rm e}^{{\rm i}S(\boldsymbol{p}_1,\boldsymbol{p}_2,\boldsymbol{k},t_3,t_2,t_1)}, \tag{24}$$

with the prefactors

$$V_{\boldsymbol{p}_2 e} = \int{\rm d}^3\boldsymbol{r}_2\Phi_{\boldsymbol{p}_2}^{(\rm V)*}(\boldsymbol{r}_2)[\boldsymbol{r}_2\cdot\boldsymbol{E}(t_3)]\psi''(\boldsymbol{r}_2), \tag{25}$$

$$V_{\boldsymbol{p}_1{\rm e},\boldsymbol{k}{\rm g}} = \iint{\rm d}^3\boldsymbol{r}_1{\rm d}^3\boldsymbol{r}_2\Phi_{\boldsymbol{p}_1}^{(\rm V)*}(\boldsymbol{r}_1)\psi''^{*}(\boldsymbol{r}_2)\frac{1}{r_{12}}\Phi_{\boldsymbol{k}}^{\mathcal{A}}(\boldsymbol{r}_1)\psi'(\boldsymbol{r}_2), \tag{26}$$

$$V_{\boldsymbol{k}{\rm g}} = \int{\rm d}^3\boldsymbol{r}_1\Phi_{\boldsymbol{k}}^{\mathcal{A}*}(\boldsymbol{r}_1)[\boldsymbol{r}_1\cdot\boldsymbol{E}(t_1)]\psi(\boldsymbol{r}_1), \tag{27}$$

and the action

$$\begin{aligned}&S(\boldsymbol{p}_1,\boldsymbol{p}_2,\boldsymbol{k},t_3,t_2,t_1)\\ &=-\int_{t_3}^{\infty}\frac{[\boldsymbol{p}_2+\boldsymbol{A}(\tau)]^2}{2}{\rm d}\tau-\int_{t_2}^{\infty}\frac{[\boldsymbol{p}_1+\boldsymbol{A}(\tau)]^2}{2}{\rm d}\tau\\ &\quad-\int_{t_1}^{\infty}\frac{[\boldsymbol{k}+\boldsymbol{A}(\tau)]^2}{2}{\rm d}\tau+E_{1{\rm g}}t_1+E_{2{\rm g}}t_2+E_{2{\rm e}}(t_3-t_2).\end{aligned} \tag{28}$$

Here, $\Phi_{\boldsymbol{k}}^{\mathcal{A}}$ ($\mathcal{A}={\rm V},{\rm CV}$) denotes either a Volkov state or a Coulomb–Volkov state. The quantities $E_{1{\rm g}}$, $E_{2{\rm g}}$, and $E_{2{\rm e}}$ represent the binding energies of the atomic ground state, the ionic ground state and the ionic exited state, respectively.

In both the SFA and ICSFA, the prefactor $V_{\boldsymbol{p}_2{\rm e}}$ is identical, while $V_{\boldsymbol{k}{\rm g}}$ is treated as a constant. The essential difference between the two frameworks arises from the rescattering cross section $V_{\boldsymbol{p}_1{\rm e},\boldsymbol{k}{\rm g}}$. In the following, we focus on a specific excitation pathway in helium, wherein laser-induced ionization of one 1s electron is followed by excitation of the remaining electron from the ionic 1s state to the 2s state.

Within the SFA, the rescattering prefactor takes the form

$$V_{\boldsymbol{p}_1{\rm e},\boldsymbol{k}{\rm g}}^{(\rm V)} = \frac{8\kappa_{\rm e}^{3/2}\kappa_{2{\rm g}}^{3/2}}{\sqrt{2}\pi}\frac{1}{(\boldsymbol{p}_1-\boldsymbol{k})^2} \times\frac{(2\kappa_{\rm e}+\kappa_{2{\rm g}})(\boldsymbol{p}_1-\boldsymbol{k})^2+(\kappa_{\rm e}+\kappa_{2{\rm g}})^2(\kappa_{2{\rm g}}-2\kappa_{\rm e})}{[(\boldsymbol{p}_1-\boldsymbol{k})^2+(\kappa_{\rm e}+\kappa_{2{\rm g}})^2]^3}, \tag{29}$$

with $\kappa_{2{\rm g}}=\sqrt{2E_{2{\rm g}}}$ and $\kappa_{\rm e}=\sqrt{2E_{2{\rm e}}}$.

Within the ICSFA, the corresponding prefactor becomes

$$V_{\boldsymbol{p}_1{\rm e},\boldsymbol{k}{\rm g}}^{(\rm CV)} = \frac{4\kappa_{\rm e}^{3/2}\kappa_{2{\rm g}}^{3/2}N_k}{(2\pi)^{3/2}} \times\Big[\Big(\frac{16\pi\kappa_{\rm e}}{\kappa^3}-\frac{4\pi}{\kappa^2}\Big)\Phi(\kappa)-\Big(\frac{4\pi\kappa_e}{\kappa^2}\Big)\frac{\rm d}{{\rm d}\kappa}\Phi(\kappa)\Big], \tag{30}$$

where

$$\begin{aligned}\Phi(\kappa) &= 8\pi[\kappa^2+(\boldsymbol{p}_1-\boldsymbol{k})^2]^{-{\rm i}\eta_k-2}\\ &\quad\times[(\boldsymbol{p}_1-\boldsymbol{k})^2+\kappa^2+2\boldsymbol{k}\cdot(\boldsymbol{p}_1-\boldsymbol{k})+2\kappa{\rm i}k]^{{\rm i}\eta_k-1}\\ &\quad\times\{-{\rm i}\eta_k(\kappa+{\rm i}k)[\kappa^2+(\boldsymbol{p}_1-\boldsymbol{k})^2]\\ &\quad+({\rm i}\eta_k+1)\kappa[(\boldsymbol{p}_1-\boldsymbol{k})^2+\kappa^2+2\boldsymbol{k}\cdot(\boldsymbol{p}_1-\boldsymbol{k})+2\kappa{\rm i}k]\},\end{aligned}$$

with $\kappa=\kappa_{2{\rm g}}+\kappa_{\rm e}$.

For both the SFA and ICSFA, the classical action S [Eq. (28)] remains identical. The multi-dimensional integrations in Eq. (24) are evaluated using the saddle-point approximation, which are obtained by extremizing the action S with respect to the variables $\boldsymbol{k},t_3,t_2,t_1$, yielding the saddle-point equations

$$[\boldsymbol{k}+\boldsymbol{A}(t_1)]^2 = -2E_{1{\rm g}}, \tag{31}$$

$$\boldsymbol{k} = -\frac{1}{t_2-t_1}\int_{t_1}^{t_2}\boldsymbol{A}(\tau){\rm d}\tau, \tag{32}$$

$$[\boldsymbol{p}_1+\boldsymbol{A}(t_2)]^2 = [\boldsymbol{k}+\boldsymbol{A}(t_2)]^2-2(E_{2{\rm g}}-E_{2{\rm e}}), \tag{33}$$

$$[\boldsymbol{p}_2+\boldsymbol{A}(t_3)]^2 = -2E_{2{\rm e}}. \tag{34}$$

Equation (31) gives the energy conservation for e_1 during the tunneling ionization. Equation (32) constrains the intermediate momentum $\boldsymbol{k}$ of e_1 so that it can return to the parent ion. Equation (33) enforces energy conservation in the recollision-induced excitation process between e_1 and e_2. Equation (34) represents the energy conservation for e_2 during the ionization from the excited state.

Since Eqs. (31) and (34) admit no real solution, the imaginary parts of $[t_1]$ and $[t_3]$ characterize the tunneling probabilities for the two electrons, with the larger imaginary components corresponding to wider tunneling barriers. For a given pair of asymptotic momentum $\boldsymbol{p}_1$ and $\boldsymbol{p}_2$, their solutions appear in complex-conjugate pairs. Throughout the analysis, the temporal ordering $t_3>t_2>t_1$ is strictly enforced to preserve the causal sequence of the RESI process.

A key quantity in the following analysis is the classification of distinct return-recollision trajectories, which are distinguished by the time interval between the ionization time t_1 and the recollision time t_2. This interval is referred to as the travel time τ. Trajectories with τ lying within the interval $nT/2\leqslant{\rm Re}\tau\leqslant(n+1)T/2$ ($n=1,2,3,\ldots$), where T denotes the optical cycle of the laser field, are identified as the nth-return-recollision trajectories [49,58]. In our calculations, the contribution of the nth-return trajectory is restricted to rescattering events in which the liberated electron approaches the parent ion multiple times but undergoes an actual collision exclusively at the nth return.

Results and Discussion

In this section, we first calculate the CEMDs using Eq. (24) with respect to the momentum components (p_{1z}, p_{2z}) along the laser polarization axis. The distributions are obtained by integrating over the transverse momentum components as well as the azimuthal angles. The external laser field is modeled as a monochromatic wave:

$$\boldsymbol{E}(t) = E_0\sin(\omega t)\widehat{\boldsymbol{e}}_z, \tag{35}$$

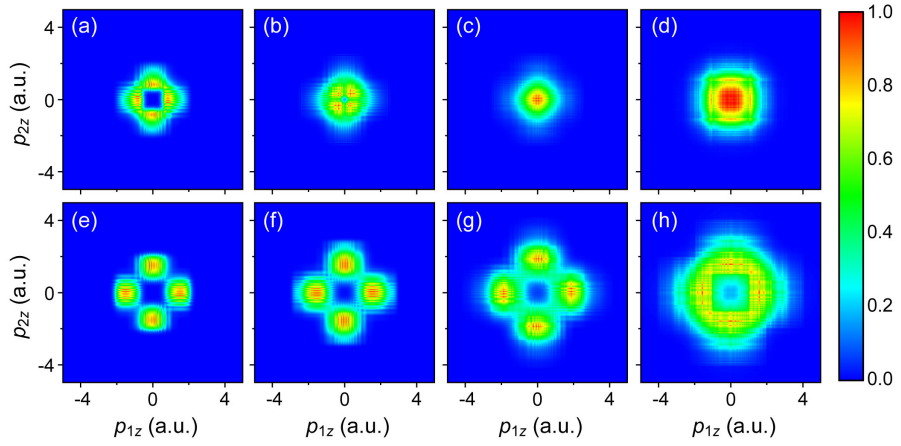

Fig. 1. Correlated electron momentum distributions (CEMDs) for helium ($E_{1g} = 0.97$ a.u., $E_{2g} = 2$ a.u., and $E_{2e} = 0.5$ a.u.) in a linearly polarized, monochromatic field of frequency $\omega = 0.057$ a.u. Driving-field intensities are: (a) and (e) $I = 2.16\times10^{14}$ W/cm^2, (b) and (f) $I = 3.0\times10^{14}$ W/cm^2, (c) and (g) $I = 5.0\times10^{14}$ W/cm^2, and (d) and (h) $I = 1.0\times10^{15}$ W/cm^2. Panels (a)–(d) are calculated by SFA method, and (e)–(h) are calculated by ICSFA method. All distributions are normalized by themselves.

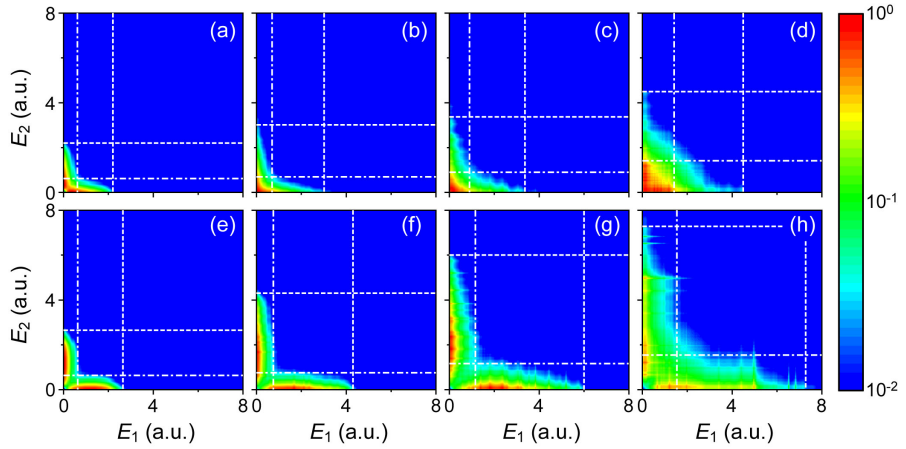

Fig. 2. Joint energy distributions (JEDs) for helium at different laser intensities. Driving-field intensities are (a) and (e) $I = 2.16\times10^{14}$ W/cm^2 [$U_p = 0.475$ a.u.], (b) and (f) $I = 3.0\times10^{14}$ W/cm^2 [$U_p = 0.66$ a.u.], (c) and (g) $I = 5.0\times10^{14}$ W/cm^2 [$U_p = 1.10$ a.u.], and (d) and (h) $I = 1.0\times10^{15}$ W/cm^2 [$U_p = 2.20$ a.u.], respectively. Panels (a)–(d) are calculated by SFA method, and (e)–(h) are calculated by ICSFA method. All distributions are normalized by themselves. The color map is scaled logarithmically. The dashed and dash-dot lines in the figure indicate the cutoff positions of the fast and slow electrons, respectively.

where $\hat{\boldsymbol{e}}_z$ denotes the unit vector along the z-axis, ω is the laser field frequency, and E_0 represents the amplitude of the electric field. And, the ponderomotive energy of the electron in the laser field is given by $U_p = E_0^2/4\omega^2$. The amplitude E_0 of the laser field, expressed in atomic units, is related to the intensity I (W/cm^2) by $I = E_0^2 I_A$, where $I_A = 3.509\times10^{16}$ W/cm^2 denotes the atomic unit of intensity.

Figure 1 displays the corresponding CEMDs for the RESI process in He driven by an 800-nm laser pulse at different intensities, as specified in the caption. The results obtained with the conventional SFA are presented in Figs. 1(a)–1(d), while those calculated by using the ICSFA are shown in Figs. 1(e)–1(h). The CEMDs are symmetrized with respect to $\boldsymbol{p}_1 \leftrightarrow \boldsymbol{p}_2$ to account for the indistinguishability of the two electrons. At an intensity of 2.16×10^{14} W/cm^2, the threshold at which the maximum return kinetic energy of e_1 is just sufficient to excite e_2, the CEMDs [see Figs. 1(a) and 1(e)] exhibit four distinct spots elongated along the p_{jz} axis. These spots constitute a characteristic signature of the dominant recollision pathways under near-threshold conditions. In this low-intensity regime, the overall shapes of the CEMDs remain largely unchanged regardless of whether the Coulomb correction is applied to the intermediate state of e_1. This consistency indicates that the electron dynamics are predominantly governed by the laser field, while the Coulomb potential plays only a secondary role.

A pronounced divergence between the results obtained from the two theoretical models emerges as the laser intensity increases. Within the SFA, which neglects the Coulomb interaction between the ionized electron and the parent ion, the CEMDs exhibit a systematic shift from the axial toward the origin. In particular, when the laser intensity reaches 5.0×10^{14} W/cm^2 and above [see Figs. 1(c) and 1(d)], the distribution maximum collapses to the center of momentum space. In contrast, the ICSFA exhibits a redistribution of the electron signal from the axial region toward higher momentum region along the axis and even into the off-axis quadrants [see Figs. 1(f)–1(h)]. Experimental measurements by Staudte *et al.* [54], together with detailed analysis by Chen *et al.* [59] for NSDI of helium driven by an 800-nm laser field at an intensity of $(4.5\pm0.5)\times10^{14}$ W/cm^2 provide a direct benchmark for these predictions. The RESI-resolved CEMDs reported in Ref. [59], which were extracted from the experimental data [54] by separating the RII and RESI contributions, display pronounced signal accumulation in high-momentum regions and in the off-axis quadrants. Notably, the ICSFA results at 5.0×10^{14} W/cm^2 [Fig. 1(g)] are in quantitative agreement with the experimental observation, accurately reproducing both the off-center location of the distribution maximum and the overall momentum-space structure.

Beyond the momentum-space dynamics, the joint energy distributions (JEDs) further elucidate the pivotal role of the Coulomb potential. Figure 2 presents the JEDs derived from the kinetic energies $E_j = \boldsymbol{p}_j^2/2$ ($j = 1,2$). Both theoretical approaches reveal an asymmetric energy sharing: one electron (slow) exhibits near-zero energy, while the counterpart (fast) carries significantly higher energy. While

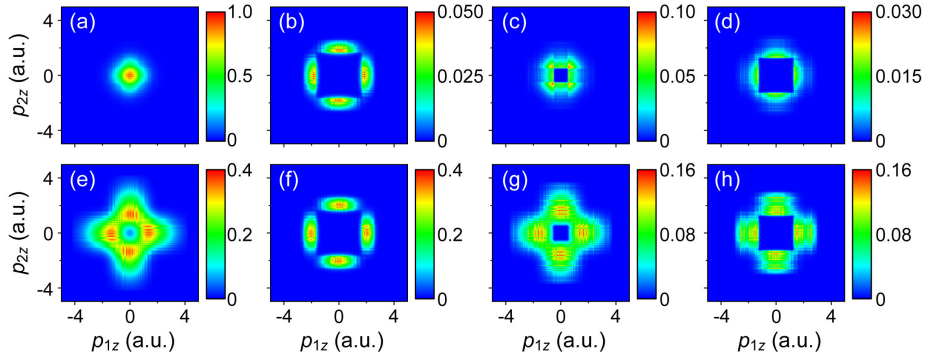

Fig. 3. CEMDs for different-return trajectories at $I = 5.0\times10^{14}$ W/cm^2. (a) and (e) are the first-return trajectories. (b) and (f) are the second-return trajectories. (c) and (g) are the third-return trajectories. (d) and (h) are the fourth-return trajectories. Panels (a)–(d) and (e)–(h) correspond to calculations using the SFA and ICSFA, respectively. All distributions are normalized by their corresponding maximum values of CEMDs in Figs. 1(c) and 1(g).

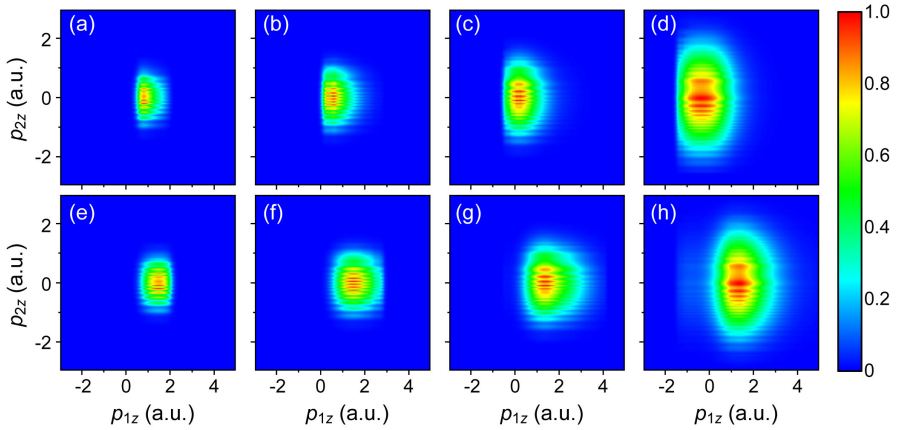

Fig. 4. Asymmetric electronic momentum distributions for the first-return trajectories at different laser intensities. Driving-field intensities are (a) and (e) $I = 2.16\times10^{14}$ W/cm^2, (b) and (f) $I = 3.0\times10^{14}$ W/cm^2, (c) and (g) $I = 5.0\times10^{14}$ W/cm^2, and (d) and (h) $I = 1.0\times10^{15}$ W/cm^2, respectively. (a)–(d) are calculated with the SFA method. (e)–(h) are calculated with the ICSFA method. All distributions are normalized by themselves.

the distribution centroids and widths evolve with increasing laser intensity, a quantitative analysis of the cutoff positions, marked by dash-dotted (slow) and dashed (fast) lines in Fig. 2, reveals stark differences between the two models.

For the slow electron, both SFA and ICSFA yield distributions peaking near zero, with widths expanding linearly with intensity, consistent with the characteristics of tunnelled electrons. Conversely, the behavior of the fast electron diverges sharply between the two frameworks. In the SFA, the spectral maximum diminishes with intensity, and despite a broadening width, the cutoff energy increases only marginally. This results in a convergence of electron energies at higher intensities, i.e., transitioning from a distinct asymmetry at low intensities toward an equal energy-sharing regime.

The ICSFA predicts a markedly different scenario. Across all intensities, both the peak positions and cutoffs of the fast-electron distribution substantially exceed SFA predictions. Notably, ICSFA reveals that the peak energy of the fast electron shifts upward with increasing laser intensity, and the cutoff extends far more rapidly than predicted by SFA. Consequently, the energy sharing remains distinctly asymmetric across the entire intensity range. This disparity underscores that the Coulomb interaction facilitates a more efficient absorption of energy from the laser field, a mechanism absent in the SFA. These energetic signatures are fully consistent with the momentum-space characteristics presented in Fig. 1.

To explore the pronounced discrepancies between the SFA and ICSFA results, we analyzed the contributions of individual MRR trajectories (from the first to the fourth return) to the CEMDs at 5.0×10^{14} W/cm^2 (as shown in Fig. 3). In SFA results, the yield from multiple return is significantly lower than that from the first return. In contrast, within the ICSFA framework, the contribution from multiple return becomes comparable to that of the first return. Beyond this general enhancement in yield, notable differences emerge in the detailed CEMDs for each return between the two models. The most striking divergence occurs in the first-return signal. Within the SFA, the first-return signal remains concentrated near the center of the momentum distribution [Fig. 3(a)], whereas the ICSFA model exhibits a pronounced shift toward larger p_{jz} values. For the second return, the distributions of the two models are nearly identical; however, for the third and fourth returns, the ICSFA distributions again shift toward higher momenta. This distinct behavior highlights the critical influence of the Coulomb potential incorporated in the ICSFA on the recollision dynamics. We proceed to dissect how the Coulomb potential reshapes the momentum and energy distribution patterns across different return-recollision trajectories and modulates their relative yields as a function of laser intensity.

To clarify the origin of this structural difference, we examine the first-return trajectories without enforcing electron indistinguishability (as shown in Fig. 4). In both models, the distribution of p_{2z} broadens with increasing intensity. The primary discrepancy arises from the evolution of the p_{1z} distribution. The SFA results [Figs. 4(a)–4(d)] demonstrate a systematic shift of the momentum distributions toward the origin (p_{jz}) with increasing laser intensity, a trend that is consistently observed across all return-recollision trajectories (not shown here). The final momentum of e_1 results from the interplay between the residual momentum transferred during the excitation of e_2 and the drift momentum imparted by the laser field. At near-threshold laser intensity [Fig. 4(a)], the final momentum is dominated by the drift momentum. However, as the intensity increases, the residual momentum (which is opposite in direction to the drift momentum due to the predominance of forward scattering in SFA) partially cancels the drift momentum, shifting the peak toward the center, thereby accounting for the observed evolution of the CEMD and JED maxima toward

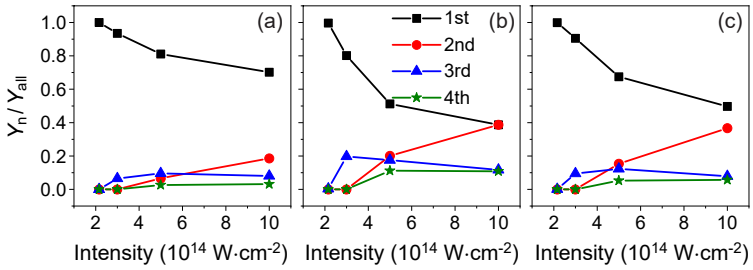

Fig. 5. Relative contributions of different return trajectories to the total CEMDs as a function of laser intensity. (a) SFA results. (b) ICSFA results. (c) ICSFA results without the N_k term.

zero in Figs. 1 and 2.

In contrast, within the ICSFA framework [Figs. 4(e)–4(h)], the intensity-dependent shift is minimal. Consequently, the resulting CEMDs retain their off-center structure. This deviation stems from the Coulomb potential's role in promoting large-angle scattering, in stark contrast to the forward scattering predicted by the SFA. Such high-angle scattering facilitates greater energy transfer, thereby displacing the electron signal toward higher-momentum regions. Consequently, the JEDs exhibit a pronounced extension toward larger energies [see Figs. 2(e)–2(h)].

As illustrated in the 'Methods' section, the saddle-point equations [Eqs. (31) to (34)] and the corresponding solutions for the MRR trajectories are identical in both models. The distinction arises solely from the rescattering prefactors $V_{p_{1e},kg}$ as defined in Eqs. (29) and (30) which determine the inelastic scattering cross-section. Consequently, the distinct structures of the CEMDs across different laser intensities between the two framework originate from fundamental differences in the differential scattering cross-section dictated by these prefactors.

In addition to altering the CEMD structure, the Coulomb potential significantly modifies the relative contributions of different recollision trajectories. Figure 5 presents the intensity-dependent relative contributions for the first to fourth returns, defined as the integrated yield of a given return normalized to the total yield. Within SFA [Fig. 5(a)], the relative contributions exhibit weak intensity dependence; the second to fourth returns consistently yield less than the first return. In contrast, the ICSFA results [Fig. 5(b)] reveal a non-monotonic evolution: the first-return contribution decreases with intensity, the second-return contribution increases and eventually rivals the first-return contribution at the highest intensity, while the third- and fourth-return contributions exhibit a rise followed by a slight decline.

Consistent with previous Coulomb-corrected studies of above-threshold ionization (ATI) [60], the enhancement of MRR trajectories in our ICSFA model is partly attributed to the Coulomb normalization coefficient N_k [Eq. (21)]. Appearing in the prefactor $V_{p_{1e},kg}$ [Eq. (30)], N_k quantifies the density of states of the intermediate wave packet and governs the strength of rescattering contributions. Since N_k increases monotonically as the intermediate canonical momentum k decreases, and multi-return trajectories are characterized by smaller k values, their contributions are inherently enhanced. This mechanism is intrinsically linked to the semiclassical Coulomb focusing effect. A smaller k corresponds to reduced kinetic energy, rendering the electron more susceptible to the attractive potential. Consequently, the Coulomb field bends the trajectory more effectively toward the parent ion, increasing the wave-packet overlap. This enhanced spatial overlap directly manifests as an increased density of intermediate states, as quantified by N_k, thereby elevating the probability of multiple returns.

To verify the aforementioned mechanism in the context of NSDI, we present results excluding the N_k term in Fig. 5(c). Compared to Fig. 5(b) (where N_k is included), the relative contributions of the second, third, and fourth returns are significantly diminished. This confirms that Coulomb focusing, manifested through N_k, enhances the yield of MRR trajectories. Nevertheless, the contributions of MRR trajectories in Fig. 5(c) remain substantially higher than those in the SFA results [Fig. 5(a)], especially for the second return. This residual enhancement indicates that other components of $V_{p_{1e},kg}$, particularly those governing the inelastic scattering cross-section, also play a crucial role. Specifically, the Coulomb potential significantly enhances the inelastic scattering cross-section in the low-energy region [57], a hallmark of Coulomb-field scattering. Since the first return possesses the highest recollision energy while the second return has the lowest, the cross-section for the second return increases dramatically, whereas that of the first return decreases. This energy-dependent enhancement is precisely observed when comparing Fig. 5(c) with Fig. 5(a). In summary, the enhanced relative contributions of MRR trajectories originate from the combined effects of Coulomb focusing (N_k) and the energy-dependent enhancement of the inelastic scattering cross-section.

Conclusion

In this work, we have derived and implemented an ICSFA theory within the framework of the IMST. By replacing the Volkov states with Coulomb-Volkov states for the recolliding electron in the intermediate stage, our formalism provides a rigorous treatment of the long-range Coulomb interaction that is typically neglected in conventional approaches.

Taking the RESI mechanism in helium as a prototypical example, we demonstrated that the inclusion of the Coulomb potential resolves critical discrepancies between theory and experiment. While the standard SFA predicts a collapse of the CEMDs toward the origin at high laser intensities, the ICSFA successfully reproduces the experimentally observed signal accumulation in high-momentum regions and off-axis quadrants. Moreover, the intermediate-state Coulomb interaction drives a substantial extension of the JED cutoff throughout the entire intensity regime.

Our analysis uncovered two distinct physical origins for the improved accuracy: (i) Coulomb focusing, manifested through the normalization coefficient N_k, increases the density of states for MRR trajectories by enhancing the wave-packet overlap with the parent ion; and (ii) Modified scattering dynamics, wherein the Coulomb potential facilitates large-angle scattering and significantly alters the energy-dependent inelastic scattering cross-section compared to the forward-scattering prediction of the SFA.

These findings highlight that the intermediate-state Coulomb interaction plays a decisive role not only in shaping the momentum distributions but also in modulating the relative weights of different recollision pathways. The ICSFA framework developed here provides a robust and computationally efficient platform for future investigations into strong-field many-body dynamics, including HHG and molecular dissociation, where electron-electron correlation and Coulomb effects are important.

It is worth noting that while the present implementation of Coulomb–Volkov states successfully captures the intermediate-state Coulomb interaction and yields qualitative agreement with experimental observations, its precision can be further refined. Drawing inspiration from the atom-Volkov SFA framework introduced in Ref. [61], future extensions could replace the approximate Coulomb–Volkov intermediate states with exact scattering states that explicitly incorporate both electron-ion and electron-electron interactions. However,

such advancements come at the cost of significantly increased computational complexity; the analytical tractability characteristic of ICSFA would likely be sacrificed in favor of extensive numerical quadrature. Therefore, future efforts will focus on synergizing the strengths of both methodologies to achieve a more rigorous yet computationally feasible description of strongly correlated electron dynamics in NSDI.

Acknowledgements

This work was supported by the National Natural Science Foundation of China (Grant Nos. 12274273, 12450402, and 12304304), Quantum Science and Technology-National Science and Technology Major Project (Grant No. 2021ZD0302101), and the Scientific and Technological Innovation Programs of Higher Education Institutions in Shanxi (Grant No. 2025Q001).

References

[1] Artemyev A N, Cederbaum L S, and Demekhin P V 2017 *Phys. Rev. A* **95** 033402
[2] Tikhomirov I, Sato T, and Ishikawa K 2017 *Phys. Rev. Lett.* **118** 203302
[3] Silva R E F, Blinov I V, Rubtsov A N, Smirnova O, and Ivanov M 2018 *Nat. Photon.* **12** 266
[4] Imai S, Ono A, and Ishiyama S 2020 *Phys. Rev. Lett.* **124** 157404
[5] Becker A, Dörner R, and Moshammer R 2005 *J. Phys. B: At. Mol. Opt. Phys.* **38** S753
[6] Figueira de Morisson Faria C, and Liu X 2011 *J. Mod. Opt.* **58** 1076
[7] Becker W, Liu X J, Ho P J, and Eberly J H 2012 *Rev. Mod. Phys.* **84** 1011
[8] Niikura H, Légaré F, Hasbani R, Bandrauk A D, Ivanov M Y, Villeneuve D M, and Corkum P B 2002 *Nature* **417** 917
[9] Niikura H, Légaré F, Hasbani R, Ivanov M Y, Villeneuve D M, and Corkum P B 2003 *Nature* **421** 826
[10] Tong X M, Zhao Z X, and Lin C D 2003 *Phys. Rev. Lett.* **91** 233203
[11] Alnaser A S, Tong X M, Osipov T, Voss S, Maharjan C M, Ranitovic P, Ulrich B, Shan B, Chang Z, Lin C D, and Cocke C L 2004 *Phys. Rev. Lett.* **93** 183202
[12] Lu P, Wang J, Li H, Lin K, Gong X, Song Q, Ji Q, Zhang W, Ma J, Li H, Zeng H, He F, and Wu J 2018 *Proc. Natl. Acad. Sci. U.S.A.* **115** 2049
[13] Hao X L, Wang J P, Zhang Z H, Qin J R, Shu Z, Li C, Zhang J Y, Li W D, He F, and Chen J 2024 *Sci. China Phys. Mech. Astron.* **67** 124205
[14] Wang J P and He F 2018 *Phys. Rev. A* **97** 043411
[15] Vrakking M J J 2021 *Phys. Rev. Lett.* **126** 113203
[16] Koll L M, Maikowski L, Drescher L, Witting T, and Vrakking M J J 2022 *Phys. Rev. Lett.* **128** 043201
[17] Vrakking M J J 2022 *J. Phys. B: At. Mol. Opt. Phys.* **55** 134001
[18] Nandi S, Stenquist A, Papoulia A *et al*. 2024 *Sci. Adv* **10** eado0668
[19] Jiang W C, Zhong M C, Fang Y K, Donsa S, Březinová I, Peng L Y, and Burgdörfer J 2024 *Phys. Rev. Lett.* **133** 163201
[20] Zhang J Y, Cao Z F, Hao X L, Li W D, and Chen J 2025 *Chin. Phys. Lett.* **42** 110301
[21] Fittinghoff D N, Bolton P R, Chang B, and Kulander K C 1992 *Phys. Rev. Lett.* **69** 2642
[22] Eichmann U, Dörr M, Maeda H, Becker W, and Sandner W 2000 *Phys. Rev. Lett.* **84** 3550
[23] Walker B, Sheehy B, DiMauro L F, Agostini P, Schafer K J, and Kulander K C 1994 *Phys. Rev. Lett.* **73** 1227
[24] Weber Th, Giessen H, Weckenbrock M, Urbasch G, Staudte A, Spielberger L, Jagutzki O, Mergel V, Vollmer M, and Dörner R 2000 *Nature* **405** 658
[25] Corkum P B 1993 *Phys. Rev. Lett.* **71** 1994
[26] Popruzhenko S V, Korneev Ph A, Goreslavski S P, and Becker W 2002 *Phys. Rev. Lett.* **89** 023001
[27] Kopold R, Becker W, Rottke H, and Sandner W 2000 *Phys. Rev. Lett.* **85** 3781
[28] Feuerstein B, Moshammer R, Fischer D *et al*. 2001 *Phys. Rev. Lett.* **87** 043003
[29] Kulander K C, Schafer K J, and Krause J L 1993 *Super-Intense Laser-Atom Physics* (SILAP) III, edited by Piraux P (Plenum, New York) **316** 95
[30] Becker A and Faisal F H M 2005 *J. Phys. B: At. Mol. Opt. Phys.* **38** R1
[31] Joachain C J 1984 *Quantum Collision Theory* (Amsterdam: North Holland)
[32] McGuire J H 1997 *Electronic Correlation Dynamics in Atomic Collisions* (Cambridge, UK: CambridgeUniversity Press)
[33] Becker A and Faisal F H M 2000 *Phys. Rev. Lett.* **84** 3546
[34] Becker A and Faisal F H M 2002 *Phys. Rev. Lett.* **89** 193003
[35] Weckenbrock M, Becker A, Staudte A, Kammer S, Smolarski M, Bhardwaj V R, Rayner D M, Villeneuve D M, Corkum P B, and Dörner R 2003 *Phys. Rev. Lett.* **91** 123004
[36] Shaaran T, Nygren M T, and Figueira de Morisson Faria C 2010 *Phys. Rev. A* **81** 063413
[37] Hao X L, Chen J, Li W D, Wang B, Wang X, and Becker W 2014 *Phys. Rev. Lett.* **112** 073002
[38] Maxwell A S and Figueira de Morisson Faria C 2016 *Phys. Rev. Lett.* **116** 143001
[39] Hao X L, Bai Y X, Li C, Zhang J Y, Li W D, Yang W F, Liu M Q, and Chen J 2022 *Commun. Phys.* **5** 31
[40] Fang Y Q, Sun F X, He Q Y, and Liu Y Q 2023 *Phys. Rev. Lett.* **130** 253201
[41] Rivera-Dean J, Stammer P, Maxwell A S, Lamprou T, Pisanty E, Tzallas P, Lewenstein M, and Ciappina M F 2024 *Phys. Rev. A* **109** 033706
[42] Rivera-Dean J, Stammer P, Figueira de Morisson Faria C, and Lewenstein M 2025 *Phys. Rev. A* **112** 063101
[43] Keldysh L V 1965 *Sov. Phys. JETP.* **20** 1307
[44] Faisal F H M 1973 *J. Phys. B: At. Mol. Opt. Phys.* **6** L89
[45] Reiss H R 1980 *Phys. Rev. A* **22** 1786
[46] Brabec T, Ivanov M Y, and Corkum P B 1996 *Phys. Rev. A* **54** 2551
[47] Yudin G L and Ivanov M Y 2001 *Phys. Rev. A* **64** 013409
[48] Moshammer R, Ullrich J, Feuerstein B *et al*. 2003 *J. Phys. B: At. Mol. Opt. Phys.* **36** L113
[49] Hao X L, Li W D, Liu J, and Chen J 2011 *Phys. Rev. A* **83** 053422
[50] Jia X Y, Hao X L, Fan D H, Li W D, and Chen J 2013 *Phys. Rev. A* **88** 033402
[51] Habibović D and Milošević D B 2025 *J. Phys. B: At. Mol. Opt. Phys.* **58** 025602
[52] Hashim S, Habibović D, and Figueira de Morisson Faria C 2025 *Phys. Rev. A* **112** 023118
[53] Hashim S, Habibović D, and Figueira de Morisson Faria C 2025 *Phys. Rev. A* **112** 023119
[54] Staudte A, Ruiz C, Schöffler M *et al*. 2007 *Phys. Rev. Lett.* **99** 263002
[55] Burgess A, Hummer D G, and Tully J A 1970 *Philos. Trans. R. Soc. London A* **266** 225
[56] Regemorter V 1960 *R. Astron. Soc.* **121** 213
[57] Shaaran T, Hatsagortsyan K Z, and Keitel C H 2018 *Phys. Rev. A* **98** 023410
[58] Figueira de Morisson Faria C, Schomerus H, and Becker W 2002 *Phys. Rev. A* **66** 043413
[59] Chen Z J, Liang Y Q, and Lin C D 2010 *Phys. Rev. A* **82** 063417
[60] Miao C L, Qin J R, Li C, Hao X L, Li W D, and Chen J 2026 *Front. Phys.* **21** 062204
[61] Milošević D B and Becker W 2019 *Phys. Rev. A* **99** 043411